A Four Port Isolated PV-Based EV Charger that Supports level-2 and DC Charging

Mohamed Tamasas Elrais Florida Power Electronics Center Florida Power Electronics Center Dept of ECE University of Central Florida Orlando, Florida, USA mohamed.elrais@knights.ucf.edu

Reza Rezaii Dept of ECE University of Central Florida Orlando, Florida, USA reza.rezaii@knights.ucf.edu

Sumana Ghosh Florida Power Electronics Center Florida Power Electronics Center Dept of ECE University of Central Florida Orlando, Florida, USA s.ghosh@knights.ucf.edu

Issa Batarseh Dept of ECE University of Central Florida Orlando, Florida, USA issa.batarseh@ucf.edu

Abstract— Electric Vehicles (EVs) that are wholly charged from renewable energy resources to avoid indirect emissions are the most effective solution for climate change and energy insecurity. This paper proposes a four-port isolated PV-based EV charging architecture that contains an LLC input stage to harvest solar energy with high efficiency because of its dual PV input ports with independent MPPT capabilities that share a common resonant tank. This architecture also includes a GaN-based flying capacitor multilevel (FCML) output stage with two GaN-based FCML converter paths, DC and AC paths. These two paths transfer power with high efficiency to two output ports, a DC port for direct DC charging and an AC port for level-2 AC charging. The system has been verified by building a 2 kW prototype module, and experimental results are presented.

Keywords—Electric vehicle (EV) chargers, photovoltaic (PV), multiport, Flying capacitor multilevel, LLC converter, level-2 charging, DC charging.

INTRODUCTION

As a result of the Electric Vehicle being an effective solution to reduce the climate change resulting from greenhouse gas emissions, electrical vehicle penetration in the modern transportation system has dramatically increased. Moreover, It is expected that in the U.S., in 2030, the electric vehicle sales percentage of the new vehicle sales in the low, medium, and high scenarios to be 2%, 12%, and 40%, respectively [1]. Globally, by 2040 the EV sales growth is expected to become more than 50% of the worldwide car sales [2]. Therefore, there is an increasing demand for charging infrastructure for EV charging. However, without harnessing sufficient solar power or any other renewable resources for charging, electric vehicles will offset any savings in carbon emissions by indirect emissions through charging from fossil fuel-generated electricity of the electric grid. There are lots of research in the literature to develop and design EV chargers and power electronics converters for other functions in the EVs to make them more reliable [3]-[5]. The Photovoltaic (PV) panels-based EV charger design is gaining popularity as the designs that combine them together can provide a green and clean alternative in the true sense. The EV charger's architectures powered by photovoltaic have been discussed in the literature [6], [7] and seem to be more demanding for the upcoming green energy era. In [6] and [8], the feasibility of charging Electric vehicles using PV without storage is discussed. A recent study in [9] indicated that charging EVs from energy generated locally by PV canopies installed in

This research is partially funded by NSF-ECCS-2103442 and NSF-ECCS-1810733.

parking lots of large retail stores is very promising and has plenty of benefits.

Motivated by the fact that EVs are an effective solution to climate change, provided true green and clean energy is used for charging, this paper proposes an isolated PV-based EV charger. This proposed charger directly charges EVs from solar PV and supports Level-2 AC and direct DC charging. It contains the dual-input LLC architecture that gives the feasibility of multiple PV sources with independent MPPT capabilities [10] and provides isolation. In addition, the proposed charger leverages the attractive GaN-based flying capacitor multilevel (FCML) design [11] to provide two types of EV charging points, level-2 AC and DC, with high efficiency. This charger is suitable for daytime charging while parking under solar canopies at large parking lots in universities and workplaces. The proposed converter architecture and operation principle of both the LLC input stage and the FCML output stage are presented in Section II. Then, the experimental verification and results are provided in section III. Finally, the conclusion is drawn in section IV.

CONVERTER ARCHITECTURE AND OPERATION **PRINCIPLE**

The proposed architecture combines the advantages of the LLC and GaN-based FCML topologies into a single PV-based EV charger module. The PV-based EV charger is constructed of two stages, the LLC input stage and the GaN-based FCML output stage that are linked through the bus capacitor, C_{bus} , as shown in Fig. 1. The operation principle of the LLC input stage is similar to the LLC resonant converter except when there is a difference in PV voltages.

A. The LLC Input Stage

In PV applications, LLC resonant converters are widely used because they have the inherent soft switching capabilities for a wide range of input voltage resulting in processing power with high efficiency[12], [13]. Moreover, LLC converters include transformers in their structures that provide the required galvanic isolation for the EV chargers. A separate conventional single input full-bridge LLC converter is required to achieve the MPPT for a single solar panel. Whereas the dual-PV LLC converter architecture deployed for the input stage in the proposed PV-based EV charger gives the feasible solution of tracking the MPPT of two solar panels, reducing the component count, decreasing the overall cost, and improving the efficiency and reliability [10], [14], [15].

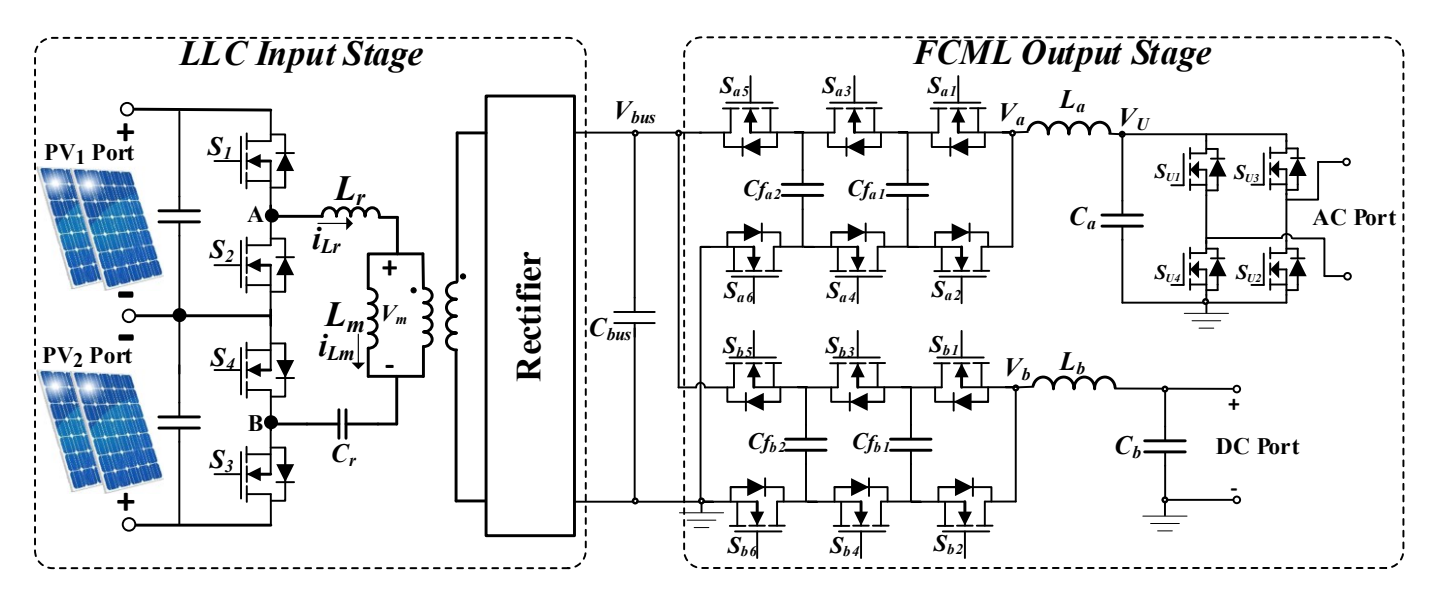


Fig. 1 The proposed two stages PV-based EV charger schematic.

In the LLC input stage of Fig. 1, two PV ports are connected to four switches arranged in two half-bridge configurations that share the same LLC resonant tank. This switching arrangement generates the square waveform at the input of the resonant tank. Both PV ports have a common ground that reduces the EMI noise. The LLC resonant tank has three components: resonant inductor (L_r) , resonant capacitor (C_r) , and magnetizing inductor (L_m) . The resonant tank is connected to the dc link through a full-bridge rectifier and a transformer with 1: n turns ratio. At the input of each port, a large capacitor is placed to keep the voltage constant across the PV terminals.

Each PV port is connected to a set of two switches of a half-bridge configuration. The PV1 port is connected to S_1 and S_2 switches set, and the PV2 port is connected to S_3 and S_4 switches set. The two switches within each set are operating in complementary PWM mode with a 50% duty cycle.

The power transfer from the LLC stage mainly depends on the switching frequency (f_s) and the phase shift (ϕ) between the PWM signals of the two sets of switches. The phase shift depends on the power mismatch between the two PV ports. Hence, the amount of power delivery varies depending on whether the phase shift between the PWM signals of the two sets of switches of the two PV ports is positive or negative. There are four switching states, which create different resonant tank voltages (V_{AB}), as illustrated in Table I.

In the switching states, it is possible that the power transfers to the output or enters free-wheeling operation mode depending

TABLE I. THE FOUR SWITCHING STATES OF THE LLC INPUT STAGE

Switches States				I/
S_I	S_2	S_3	S_4	V_{AB}
ON	OFF	OFF	ON	V_{PVI}
OFF	ON	ON	OFF	V_{PV2}
ON	OFF	ON	OFF	$V_{PVI} - V_{PV2}$
OFF	ON	OFF	ON	0

on the resonant inductor current (i_{Lr}) and magnetizing inductor current (i_{Lm}). As an example, the operation waveforms of the LLC input stage with a positive phase shift are shown in Fig. 2; in this case, the converter works in six different modes of operation in one switching cycle. These six modes are shown in Fig. 3.

Mode I (t_0 - t_1): In this mode, S_I and S_4 are ON, and PV1 is the input voltage source. The energy of PV1 is transferred to the load side since the resonant inductor current is greater than the magnetizing current. The voltage across the magnetizing inductor is constant and related to the output voltage, so the magnetizing current start to increase with a constant slope. The operation of the LLC input stage in this mode is shown in Fig. 3(a). According to the resonant components in the equivalent circuit of this positive or P mode, the resonant frequency (f_r) is equal to:

$$f_r = \frac{1}{2\pi\sqrt{L_r C_r}}\tag{1}$$

Mode II $(t_1 - t_2)$: The switches S_I and S_4 will remain ON in this mode. However, there is no output power flow to the load side since the resonant current is same as the magnetizing current, shown in Fig. 3(b). This means the converter is in the free-wheeling mode forming O-mode.

Mode III (t_2-t_3): In this mode, the input of the resonant tank is PV1 – PV2 since S_1 and S_3 are ON. Similar to the previous mode, the energy does not transfer to the load side because the resonant and magnetizing currents are equal. This mode is called the phase shifted mode or S-mode of the LLC input stage and it is shown in Fig. 3(c).

Mode IV (t_3 - t_4): The switches S_2 and S_3 are ON in this mode, and PV2 is the input voltage source. The energy of PV2 is transferred to the load side because the resonant current is greater than the magnetizing current. This is a negative or N mode operation of the LLC input stage, and the circuit diagram is shown in Fig. 3(d).

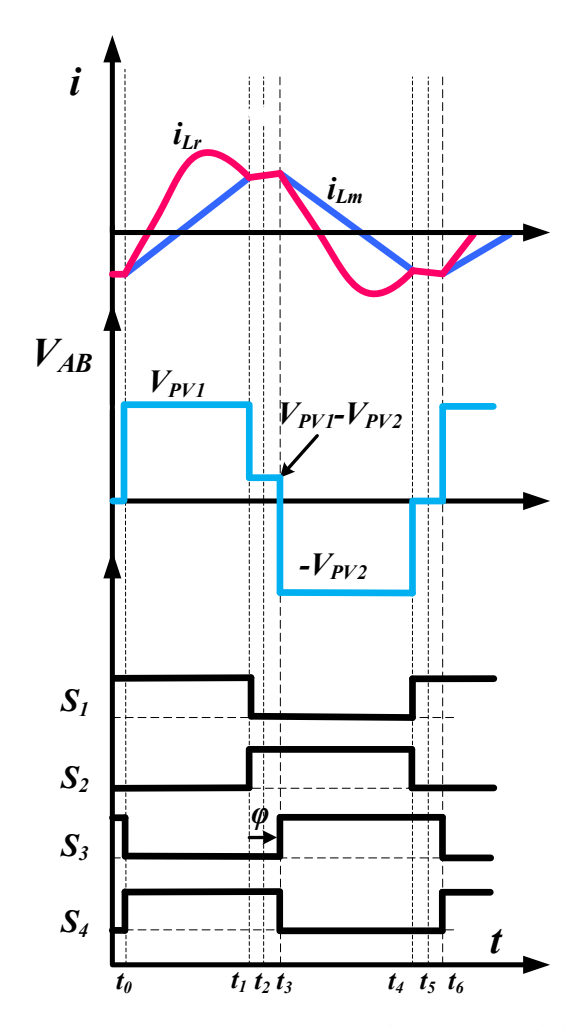


Fig. 2 LLC Input stage operation waveforms with positive phase-shift.

Mode V (t_4 - t_5): The switches S_2 and S_3 will remain ON in this mode. However, there is no output power flow to the load side since the resonant current is the same as the magnetizing current, as shown in Fig. 3(e). This means the converter is in the free-wheeling mode forming O-mode.

Mode VI (t_5 - t_6): In this mode, the input of the resonant tank is zero since S_2 and S_4 are ON. Same as the previous mode, the energy does not transfer to the load side because the resonant current and magnetizing current are equal. In this mode, the magnetizing inductor is a part of the resonant circuit, which means the magnetizing current does not change with a constant slope. The operation of the LLC input stage in this mode is shown in Fig. 3(f). According to the resonant components in the equivalent circuit of this phase shifted mode or S mode of the LLC input stage, the resonant frequency is equal to:

$$f_m = \frac{1}{2\pi\sqrt{(L_r + L_m)C_r}}\tag{2}$$

B. The FCML Output Stage

As can be seen in Fig. 1, the FCML output stage contains a DC path and an AC path. Each path is a 4-level FCML that

contains 2(N-1) switches, when N the number of levels equals 4, that is six switches S_{b1} , S_{b2} , S_{b3} , S_{b4} , S_{b5} , and S_{b6} for the DC path and six switches S_{a1} , S_{a2} , S_{a3} , S_{a4} , S_{a5} , and S_{a6} for the AC path. Gallium Nitride (GaN) switches are used for all these twelve switches for their low gate charge that result in lower switching losses compared to MOSFET switches [16], and they switch at a switching frequency (f_s) equals 120 kHz and block only a fraction of the bus voltage of $\frac{V_{bus}}{N-1} = \frac{V_{bus}}{3}$.

Each path contains (N-2) flying capacitors which are two flying capacitors Cf_{a1} and Cf_{a2} for the AC path, and Cf_{b1} and Cf_{b2} for the DC path. The voltages across the flying capacitors are naturally balanced to the desired values by controlling the switches using the Phase Shifted Pulse Width Modulation (PSPWM)[17], [18]. The desired voltages across the flying capacitors are determined by

$$V_{Cf_{xy}} = \frac{y \times V_{bus}}{N-1},\tag{3}$$

where x = (a, b) and y = (1, 2), which are $V_{Cf_{a1}} = V_{Cf_{b1}} = \frac{1*V_{bus}}{N-1}$, and $V_{Cf_{a2}} = V_{Cf_{b2}} = \frac{2*V_{bus}}{N-1}$.

The AC path includes a full-bridge unfolder that uses MOSFET switches S_{U1} , S_{U2} , S_{U3} , and S_{U4} that switch at 60 Hz to generate the AC voltage [11], [19].

The maximum filtering inductance value required to keep the inductor current ripple (Δ_{i_L}) within its designed limit that is specified by the design is calculated for both DC and AC paths as [19]

$$L = \frac{0.25 \, V_{bus}}{\Delta_{i_L} \times f_s \times (N-1)^2} \tag{4}$$

As can be seen in (4), as the number of levels N increases, the filtering inductance value decreases accordingly by a factor of $(N-1)^2$; this inductance reduction resulted from the frequency multiplication effect seen by the inductor and the voltage swing reduction across the inductor, which are two very beneficial features of the FCML topology. It should be noted that this $(N-1)^2$ inductance reduction is the factor by which the required inductance of the flying capacitor multilevel topology is smaller than the required inductance for the two-level conventional topology when both topologies work at the same switching frequency, inductor's current ripple, and input voltage [18]–[20].

The flying capacitors in both the DC and AC paths are the main power transfer elements, and their value can be determined as

$$Cf = \frac{I_{load}}{\Delta V_{cf} \times f_s \times (N-1)}$$
 (5)

where ΔV_{Cf} is the flying capacitor voltage ripple and I_{load} is the DC load current for the DC path and the peak load current for the AC path [18], [19], [21].

In the DC path, the switches are controlled using the PSPWM, in which the PWM signals of the three switches S_{b1} , S_{b3} , and S_{b5} are shifted from each other by $\frac{360}{N-1}$ or 120° and

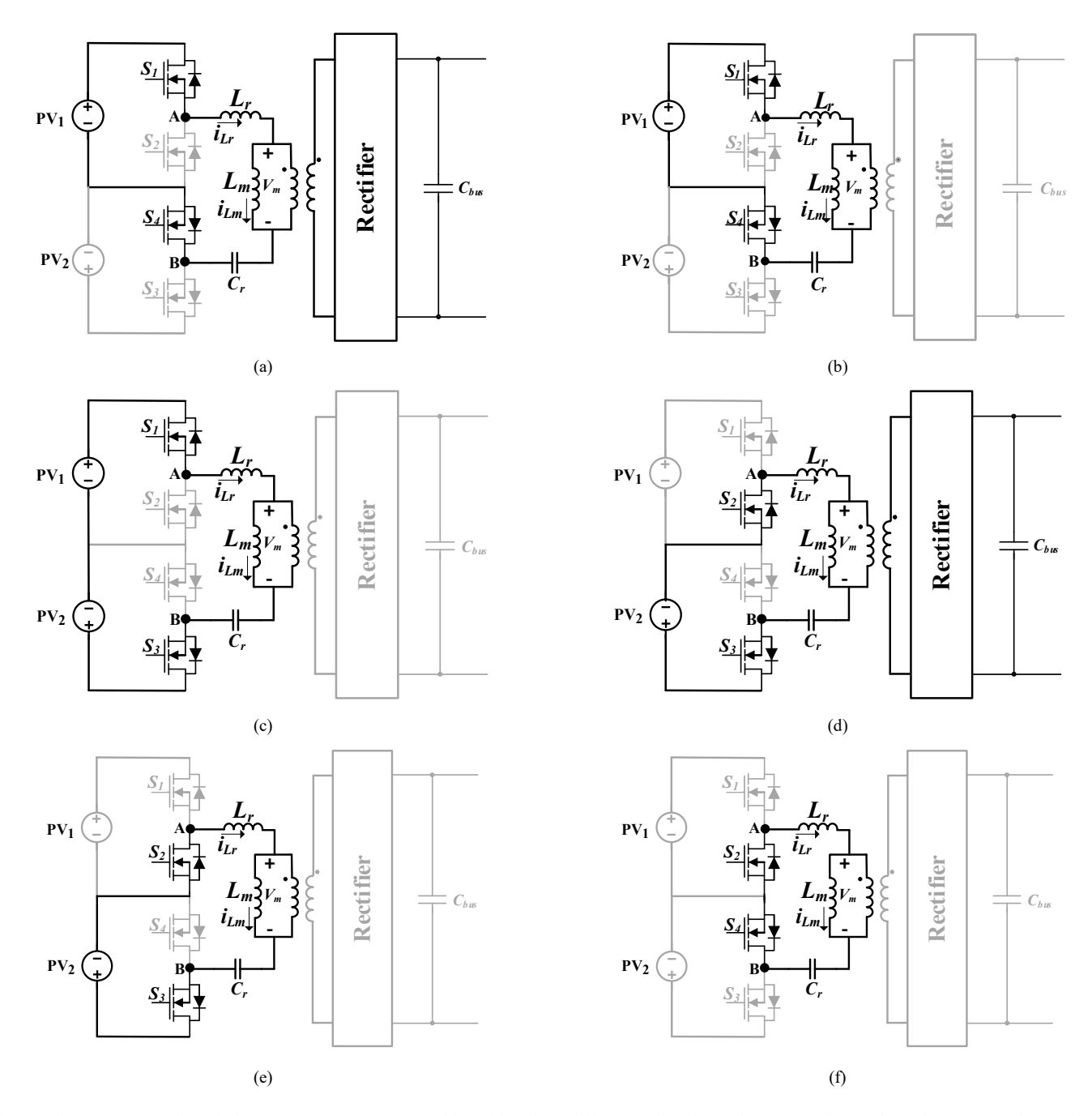


Fig. 3. The operation modes of the LLC resonant input stage with positive phase-shift (a) Mode I, (b) Mode II, (c) Mode III, (d) Mode IV, (e) Mode V, and (f) Mode VI.

have a fixed duty cycle D. The other three switches S_{b2} , S_{b4} , and S_{b6} are working in a complementary way with a duty cycle of (1-D). The switching node voltage V_b is a pulsed width modulated waveform that is switching at 360 kHz, which is seen by the inductor L_b . This switching node voltage V_b is filtered by L_b and C_b to produce a pure DC voltage at the DC Port

In the AC path, the switches are controlled using the PSPWM, in which the PWM signals of the three switches S_{a1} , S_{a3} , and S_{a5} are shifted from each other by $\frac{360}{N-1}$ or 120° .

Unlike the DC path, they have a varying duty cycle D that follows a rectified sinewave reference to generate the switching node voltage V_a which is a pulsed four-level staircase rectified sinewave voltage that is switching between two levels of the four-level staircase waveform at 360 kHz. This pulse frequency of the four-level staircase rectified sinewave voltage is three times the switching frequency of each switch and is seen by the inductor L_a . The other three switches S_{a2} , S_{a4} , and S_{a6} are working in a complementary way. The four-level staircase switching node voltage V_a is filtered by L_a and C_a to produce a clean full-wave rectified sinewave at the node voltage V_U .

Finally, the clean full-wave rectified sinewave at node V_U is unfolded every 1/120 of a second by the full-bridge unfolder to generate a sinusoidal AC voltage of 240 V_{rms} at the AC port.

III. EXPERIMENTAL RESULTS

A 2 kW prototype is built to verify the PV-based EV charger performance; the LLC input stage can process a maximum power of 2 kW, and each of the DC and AC paths of the FCML output stage can process a maximum power of 2 kW. In order to test the operation of the LLC input stage in the worst case scenarios, a power mismatch is applied to the two PV sources. In this scenario, the irradiation on PV2 is 400 W/m^2 which is half of the PV1. In other words, the power of the PV2 is reduced by shading. In this situation, the LLC input stage can track the MPP of each PV source individually by applying phase-shift to PWM switching signals. Fig. 4 shows the S_I and S_3 switches' PWM signals with a negative phase shift (φ). According to this negative phase shift, most of the power is delivered by PV1.

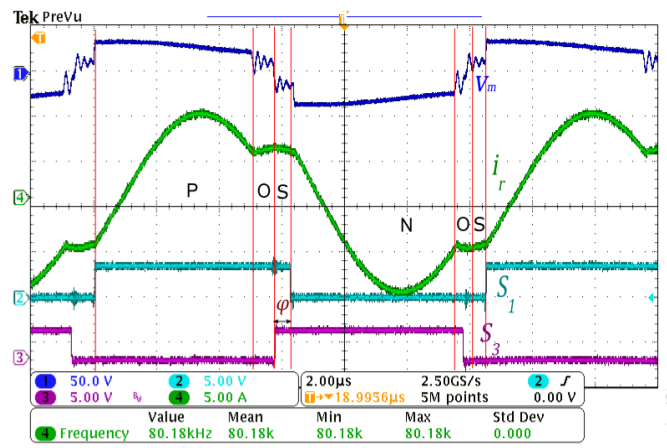


Fig. 4 The waveforms when solar irradiance,G1 > G2 at f_s = 80 kHz and φ = -26° (CH1: V_m , CH2: S_l gate signal, CH3: S_3 gate signal, CH4: i_{Lr}) for POS-NOS switching cycle.

The switching frequency of the LLC input stage in this test is 80 kHz, which is less than the resonant frequency of 100 kHz. In addition, the resonant waveforms of the magnetizing voltage, V_m , resonant inductor current, i_{Lr} , are shown in Fig. 4. All operation modes of the previously discussed LLC input stage are shown in the resonant waveforms in Fig. 4.

The I-V and P-V curves of both PV sources are extracted by solar array simulators (SAS) software, as shown in Fig. 5.

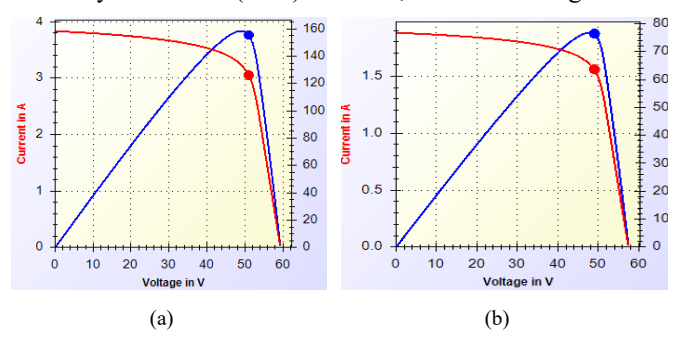


Fig. 5 P-V and I-V curves of the PV sources (a) PV1 with G=800 W/m2, (b) PV2 with G=400 W/m2.Fig. 6 P-V and I-V curves of the PV sources (a) PV1 with G=800 W/m2, (b) PV2 with G=400 W/m2.

Both PVs are tracking their MPP, and they are working separately. The LLC input stage has achieved an efficiency of 96 %.

The output voltage and current of the DC port at 1.8 kW are shown in Fig. 7. The four-level staircase switching node voltage V_a , and the filtered rectified sinewave at node V_U , are shown in Fig. 8. The equal $\frac{V_{bus}}{N-1} = \frac{450}{3} = 150 \text{ V}$ step increments of the staircase voltage waveform indicate well-balanced voltages across the flying capacitors in the AC path. The output voltage and current of the AC port at 1.436 kW are shown in Fig. 9.

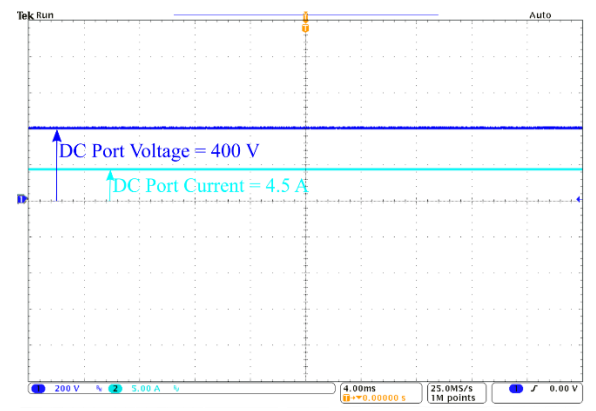


Fig. 7. The output voltage and current of 400~V and 4.5A of the DC port at 1.8kW.

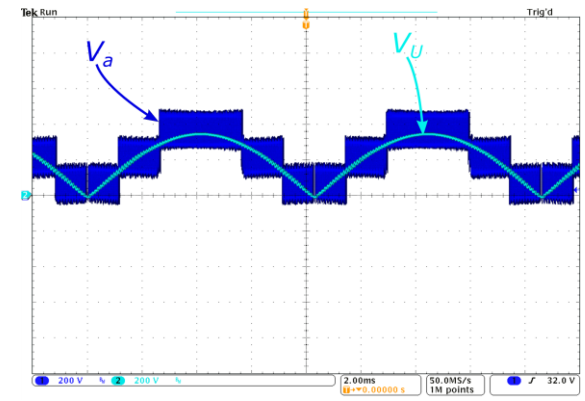


Fig. 8. The four-level staircase switching node voltage V_a and and the filtered rectified sinewave at node V_{tt} .

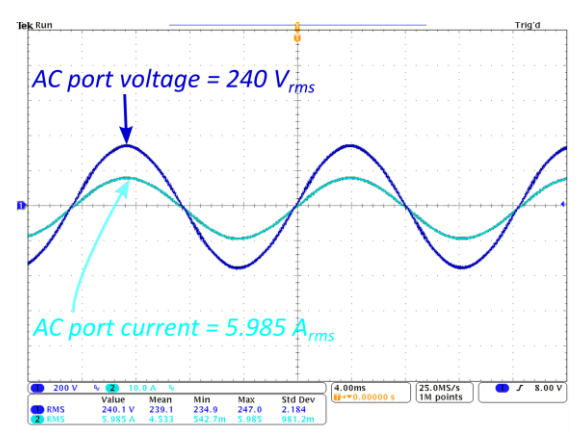


Fig. 9. The output voltage and current of 240 V_{rms} and $5.985A_{\text{rms}}$ of the AC port at 1.436 kW.

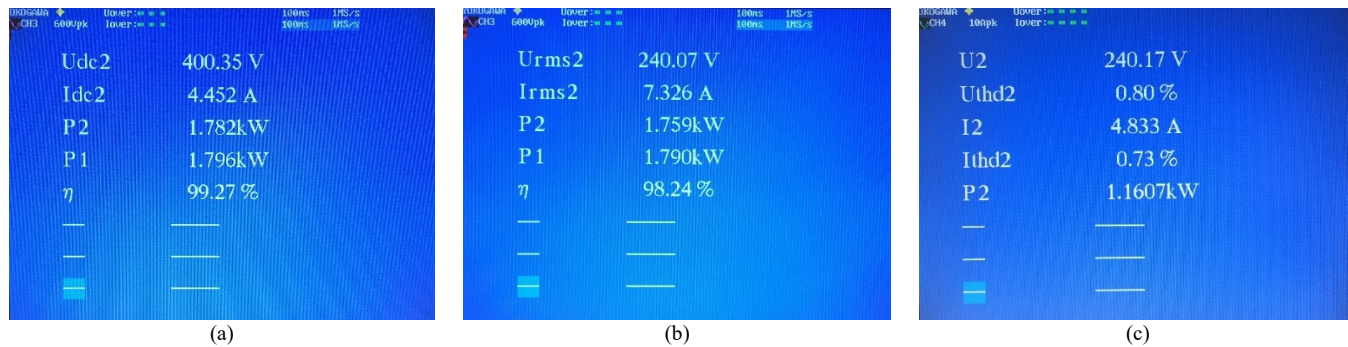


Fig. 10. (a) Udc2 and Idc2 are the DC port voltage and current, P2 and P1 are the DC path output and input power, and η is the efficiency of the DC path. (b) Urms2 and Irms2 are the AC port RMS voltage and current, P2 and P1 are the AC path output and input power, and η is the efficiency of the AC path. (c) U2 and I2 are the AC port RMS voltage and current, Uthd2 and Ithd2 are the THD of the AC port's voltage and current and P2 is the AC output power.

Fig. 10. shows three photos of the YOKOGAWA PZ4000 POWER ANALYZER screen as follows (a) the DC path peak efficiency of 99.27 %; (b) the AC path peach efficiency of 98.24 %; (c) the THD of the AC port voltage and current of 0.8% and 0.73%, respectively.

IV. CONCLUSION

Moved by the fact that electric vehicles are considered environmentally friendly only if they charge from green renewable energy resources, this paper presented a four-port isolated PV-based EV charging system that supports DC and level-2 AC charging. It consists of two stages, an LLC input stage that supports two PV inputs with independent MPPT capabilities and an FCML output stage that provide DC and level-2 AC charging points. The proposed charger charges electric vehicles directly from local PV panels generation. An ideal application for this charger is charging EVs from solar canopies during daylight at parking lots. The charger functionality has been verified theoretically and experimentally. Experimental results indicating this charger's promising potential are provided through testing a 2 kW hardware prototype.

REFERENCES

- [1] U.S Department of Energy "Summary Report on EVs at Scale and the U.S. Electric Power System", November 2019. https://www.energy.gov/
- [2] BloombergNEF, "Electric Vehicle Outlook 2020," Tech. Rep., 2020. [Online]. Available: https://about.bnef.com/electric-vehicle-outlook/
- [3] M. Safayatullah, M. T. Elrais, S. Ghosh, R. Rezaii, and I. Batarseh, "A Comprehensive Review of Power Converter Topologies and Control Methods for Electric Vehicle Fast Charging Applications," *IEEE Access*, vol. 10, pp. 40753–40793, 2022.
- [4] R. Rezaii, M. Nilian, M. Safayatullah, S. Ghosh, and I. Batarseh, "A Bidirectional DC-DC Converter with High Conversion Ratios for the Electrical Vehicle Application," *IECON Proc. (Industrial Electron. Conf.*, vol. 2021-Octob, pp. 0–5, 2021.
- [5] R. Rezaii, M. Nilian, M. Safayatullah, F. Alaql, and I. Batarseh, "Design and Experimental Study of A High Voltage Gain Bidirectional DC-DC Converter for Electrical Vehicle Application," pp. 2058–2063, 2022.
- [6] S. Khan, A. Ahmad, F. Ahmad, M. Shafaati Shemami, M. Saad Alam, and S. Khateeb, "A Comprehensive Review on Solar Powered Electric Vehicle Charging System," *Smart Sci.*, vol. 6, no. 1, pp. 54–79, 2018.
- [7] G. R. C. Mouli, P. Bauer, and M. Zeman, "Comparison of system architecture and converter topology for a solar powered electric vehicle charging station," 9th Int. Conf. Power Electron. - ECCE Asia "Green World with Power Electron. ICPE 2015-ECCE Asia, pp. 1908–1915, 2015.

- [8] S. Lee, S. Iyengar, D. Irwin, and P. Shenoy, "Shared solar-powered EV charging stations: Feasibility and benefits," 2016 7th Int. Green Sustain. Comput. Conf. IGSC 2016, pp. 0–7, 2017.
- [9] S. S. Deshmukh and J. M. Pearce, "Electric vehicle charging potential from retail parking lot solar photovoltaic awnings," *Renew. Energy*, vol. 169, pp. 608–617, 2021.
- [10] A. Alhatlani, S. Ghosh, I. Batarseh, and N. Kutkut, "Exact Steady-State Analysis of Phase-Shifted Dual-Input LLC Converter," in 2019 IEEE Energy Conversion Congress and Exposition, ECCE 2019, 2019, pp. 1394–1400.
- [11] M. T. Elrais and I. Batarseh, "Design and Experimental Study of a GaN-based Three-Port Multilevel Inverter," in IECON 2021 47th Annual Conference of the IEEE Industrial Electronics Society, 2021, pp. 1–6.
- [12] F. Alaql, R. Rezaii, S. Gullu, M. T. Elrais, and I. Batarseh, "A Switchable Rectifier-based LLC Resonant Converter for Photovoltaic Applications," 2021 IEEE Energy Convers. Congr. Expo. ECCE 2021 - Proc., pp. 2093– 2098, 2021.
- [13] S. Ghosh, M. Safayatullah, M. T. Elrais, and I. Batarseh, "A Novel Four-port LLC Converter for Dual PV and Battery Integration," *IECON Proc. (Industrial Electron. Conf.*, vol. 2021-October, 2021.
- [14] S. M. Tayebi, H. Hu, S. Abdel-Rahman, and I. Batarseh, "Dual-Input Single-Resonant Tank LLC Converter with Phase Shift Control for PV Applications," *IEEE Trans. Ind. Appl.*, vol. 55, no. 2, pp. 1729–1739, 2019.
- [15] S. Ghosh and I. Batarseh, "Grid-tied Two PV LLC Converter with Dual MPPT Algorithm based on the Adaptive Neuro Fuzzy Interface System (ANFIS)," 2021 IEEE Energy Convers. Congr. Expo. ECCE 2021 - Proc., pp. 3007–3013, 2021.
- [16] M. Safayatullah, W. Yang, J. S. Yuan, and B. Krishnan, "Switching loss characterization of GaN-based buck converter under different substrate biases," in 2019 IEEE 7th Workshop on Wide Bandgap Power Devices and Applications, WiPDA 2019, 2019, pp. 374–377.
- [17] B. P. McGrath and D. G. Holmes, "Natural capacitor voltage balancing for a flying capacitor converter induction motor drive," *IEEE Trans. Power Electron.*, vol. 24, no. 6, pp. 1554–1561, 2009.
- [18] M. T. Elrais and I. Batarseh, "A GaN Based Four-Port Flying Capacitor Multilevel Converter," 2021 IEEE Energy Convers. Congr. Expo. ECCE 2021 - Proc., pp. 2480–2486, 2021.
- [19] Y. Lei et al., "A 2-kW Single-Phase Seven-Level Flying Capacitor Multilevel Inverter with an Active Energy Buffer," *IEEE Trans. Power Electron.*, vol. 32, no. 11, pp. 8570–8581, 2017.
- [20] Q. Huang, Q. Ma, P. Liu, A. Q. Huang, and M. A. De Rooij, "99% Efficient 2.5-kW four-level flying capacitor multilevel GaN totem-pole PFC," *IEEE J. Emerg. Sel. Top. Power Electron.*, vol. 9, no. 5, pp. 5795–5806, 2021.
- [21] C. B. Barth et al., "Design and Control of a GaN-Based, 13-Level, Flying Capacitor Multilevel Inverter," IEEE J. Emerg. Sel. Top. Power Electron., vol. 8, no. 3, pp. 2179–2191, 2020.